Competitive superconductivity and charge density wave in Mo-doped kagome superconductor CsV_3Sb_5

K. J. Zhu,[1,*] L. P. Nie,[2,*] B. Lei,[1] M. J. Wang,[1] K. L. Sun,[2] Y. Z. Deng,[1] M. L. Tian,[1] T. Wu,[2,3,4,5,†] and X. H. Chen[2,3,4,5,‡]

[1]*School of Physics and Optoelectronic Engineering, Anhui University, Hefei, Anhui 230601, China*
[2]*Hefei National Research Center for Physical Sciences at the Microscale, University of Science and Technology of China, Hefei, Anhui 230026, China*
[3]*CAS Key Laboratory of Strongly-coupled Quantum Matter Physics, Department of Physics, University of Science and Technology of China, Hefei, Anhui 230026, China*
[4]*Collaborative Innovation Center of Advanced Microstructures, Nanjing University, Nanjing 210093, China*
[5]*Hefei National Laboratory, University of Science and Technology of China, Hefei 230088, China*

(Received 4 September 2023; accepted 20 May 2024; published 20 June 2024)

In the kagome superconductors AV_3Sb_5 (A = K, Rb, Cs), understanding the charge-density-wave (CDW) state and its entanglement with the superconducting ground state is still a challenging issue. Here, by measuring the electrical transport, magnetic susceptibility, Hall effect, and ^{51}V nuclear magnetic resonance (NMR), the evolution of superconductivity (SC) and the CDW is comprehensively studied in $Cs(V_{1-x}Mo_x)_3Sb_5$. In contrast with previously reported results for other doped cases, the CDW transition temperature slightly increases to ~100 K with increasing Mo doping. Meanwhile, the SC is quickly suppressed and vanishes above $x = 0.02$. The anomalous Hall effect (AHE), which is tied to the exotic nature of the CDW state in pristine CsV_3Sb_5, is also strongly suppressed and completely disappears above $x = 0.07$. Further ^{51}V NMR investigation on the CDW state in $Cs(V_{0.95}Mo_{0.05})_3Sb_5$ indicates that a short-range stripelike CDW evolves from the original triple-Q CDW state with increasing Mo doping, which largely reduces the density of states at the Fermi level. This result provides a self-consistent explanation for the disappearance of both SC and the AHE by increasing Mo doping, which offers insights into the competitive behavior between SC and the CDW state in the kagome superconductors AV_3Sb_5.

DOI: 10.1103/PhysRevResearch.6.023295

I. INTRODUCTION

Due to geometrical frustration, the band structure of a two-dimensional (2D) kagome lattice hosts flat bands, saddle points, and Dirac points, which is a fertile platform for correlated and topological electronic states [1–7]. Recently, a kagome superconductor family AV_3Sb_5 (A = K, Rb, Cs) was discovered and successfully attracted significant attention [8–13]. In AV_3Sb_5, above the superconducting temperature ($T_c \sim 0.9-3$ K), a triple-Q charge-density-wave (CDW) state with an in-plane $2a \times 2a$ structural modulation occurs through a first-order structural transition with the CDW transition temperature (T_{CDW}) ranging from ~80 to 104 K in different materials [8–10]. Meanwhile, a giant anomalous Hall effect (AHE) was simultaneously observed in the CDW state, suggesting a possible time-reversal symmetry breaking (TRSB) [14,15]. More evidence from muon spin rotation (μSR) and scanning tunneling microscopy (STM) experiments further supports TRSB in the CDW state [16–21]. Theoretically, a so-called chiral flux phase has been proposed to explain the possible TRSB in AV_3Sb_5 [22], in which the time-reversal symmetry is broken by the loop-current order like that proposed in high-T_c cuprates [23]. Nonetheless, whether the TRSB is an intrinsic property of the CDW state is still under debate [24–27]. In addition to the possible TRSB, the electronic nematicity, which is beyond a simple rotational symmetry breaking due to the three-dimensional (3D) CDW structure, was also revealed inside the CDW states below a characteristic temperature $T_{nem} \sim 35$ K in CsV_3Sb_5 [28,29]. Interestingly, further nuclear magnetic resonance (NMR) study indicated that such an electronic nematicity evolves into a stripelike CDW by applying a hydrostatic pressure above a critical value $P_c \sim 0.58$ GPa [30], which leads to the two-dome-shaped superconducting phase diagram in pressurized CsV_3Sb_5 [30–32]. All these results point out the extraordinary nature of the CDW state in kagome superconductors AV_3Sb_5, which remains an open issue at the present stage.

Chemical doping is an efficient way to tune both CDW and superconductivity (SC). In previous studies, the chemical doping effect has been investigated in several doped kagome superconductors, such as $Cs(V_{1-x}B_x)_3Sb_5$ (B = Ti, Cr, Nb, Mo, Ta) and $CsV_3Sb_{5-x}Sn_x$ [33–41]. In their

*These authors contributed equally to this work.
†Contact author: wutao@ustc.edu.cn
‡Contact author: chenxh@ustc.edu.cn

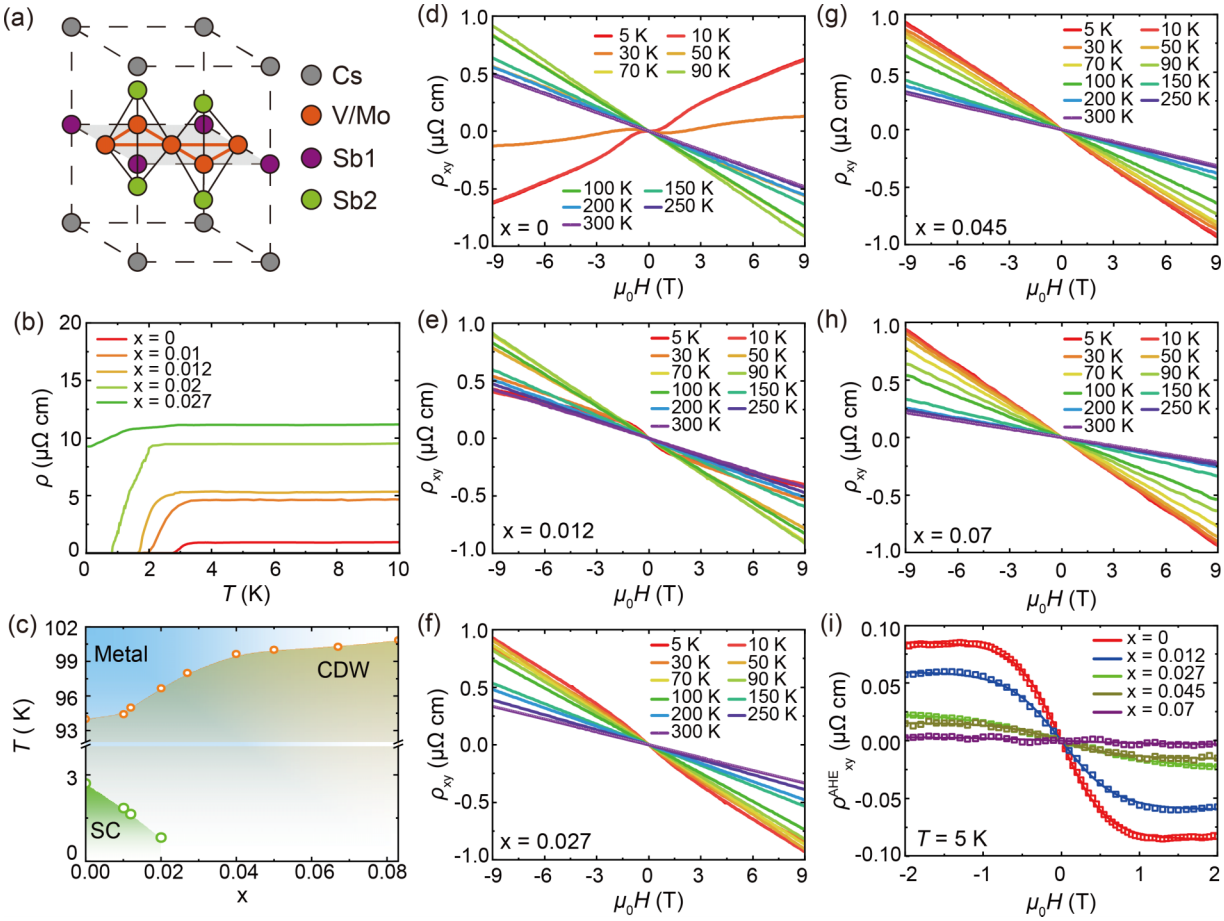

FIG. 1. (a) Crystal structure of $Cs(V_{1-x}Mo_x)_3Sb_5$. The bulk single crystal of CsV_3Sb_5 exhibits a layered structure consisting of V_3Sb_5 layers stacked between Cs layers. (b) The evolution of superconducting transition temperatures in resistivity curves for low Mo doping. T_c decreases monotonically with Mo doping. (c) Phase diagram of $Cs(V_{1-x}Mo_x)_3Sb_5$ which illustrates the competition between the charge density wave (CDW) and superconductivity (SC). Here, T_c is defined as the zero-resistance temperature. (d)–(h) Field dependence of the Hall resistivity (ρ_{xy}) at various temperatures for $Cs(V_{1-x}Mo_x)_3Sb_5$ single crystals from 5 to 300 K with (d) $x = 0$, (e) $x = 0.012$, (f) $x = 0.027$, (g) $x = 0.045$, and (h) $x = 0.07$. (i) Extracted ρ_{xy}^{AHE} taken by subtracting the linear ordinary Hall background at 5 K for Mo doping contents from $x = 0$ to 0.07. The anomalous Hall effect (AHE) was significantly weakened with Mo doping.

doping-dependent phase diagrams, T_{CDW} is always suppressed monotonically while the AHE is strongly suppressed and exhibits an intimate correlation with the CDW state [34,36,37]. In contrast to the simple doping-dependent behavior of T_{CDW}, the doping-dependent T_c shows rather complicated behaviors. In the Nb- and Ta-doped cases, T_c increases with increasing the doping level [37–41]. In the Cr- and Mo-doped cases, T_c decreases with increasing the doping level [36,41]. In the Ti- and Sn-doped cases, T_c exhibits a two-domelike behavior with increasing doping level [33–35], which is like that in pressurized CsV_3Sb_5 [30–32]. The correlation between CDW and SC in these doped cases remains elusive and under strong debate [42,43]. It should be noted that, among all the above doped cases, Mo-doped CsV_3Sb_5 is quite unique. In this case, T_{CDW} increases with increasing Mo-doping level, while T_c decreases monotonically, which suggests a strong competition between the CDW and SC. Here, by utilizing AHE and NMR measurements, we clarify the correlation between CDW and SC in Mo-doped CsV_3Sb_5. Our results reveal that the emergence of a stripelike CDW modulation with the introduction of Mo doping causes the disappearance of the AHE and the strong competition between the CDW and SC.

II. EXPERIMENTAL RESULTS

High-quality single crystals of $Cs(V_{1-x}Mo_x)_3Sb_5$ were synthesized via a self-flux method with molybdenum doping ($0 \leqslant x \leqslant 0.083$). The crystal structure, where the V/Mo atoms formed a 2D kagome network, is presented in Fig. 1(a). Figure 1(b) shows the superconducting behavior by measuring the low-temperature $\rho(T)$ curves for $Cs(V_{1-x}Mo_x)_3Sb_5$. Continuous Mo doping leads to the remarkable suppression of SC. The phase diagram of $Cs(V_{1-x}Mo_x)_3Sb_5$ is summarized in Fig. 1(c), where the SC and CDW transition is determined by resistance measurements (Fig. S1 in the Supplemental Material (SM) [44]). Remarkably, as the doping level increases, T_{CDW} also increases and reaches 100.9 K at the highest doping content of $x = 0.083$, which was also confirmed by magnetization (Fig. S2(a) in the SM [44]) and specific heat measurements (Figs. S2(b) and S2(c) in the SM [44]). Meanwhile, T_c drops quickly to zero above $x = 0.02$. All the above

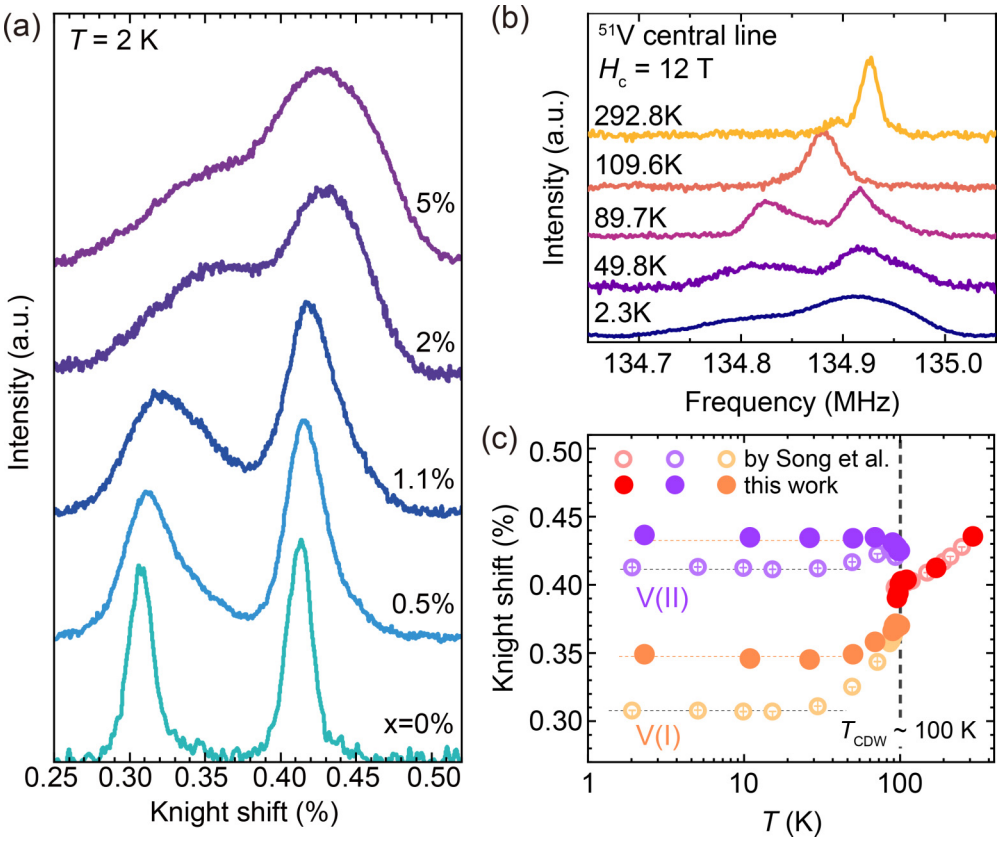

FIG. 2. (a) Mo-doping-dependent nuclear magnetic resonance (NMR) spectra at 2 K with an external magnetic field $\mu_0 H = 12$ T along the crystalline c axis. (b) Temperature-dependent ^{51}V ($\frac{1}{2} \leftrightarrow -\frac{1}{2}$) NMR transition lines for $Cs(V_{0.95}Mo_{0.05})_3Sb_5$. (c) Temperature-dependent Knight shift for pristine (open dots) [48] and Mo-doped CsV_3Sb_5 (solid dots). Below T_{CDW}, we defined the low-frequency peak as the V(I) site (yellow) and the other as the V(II) site (violet).

results suggest a strong competition between CDW and SC in Mo-doped CsV_3Sb_5.

To elucidate the origin of the above competitive behavior between the CDW and SC, we further study the doping-dependent evolution of the AHE which is thought to be intimately correlated with the CDW in pristine and doped AV_3Sb_5 [14,15,34,36,37,45]. Figure 1(d) shows the field-dependent Hall resistivity (ρ_{xy}) at various temperatures in pristine CsV_3Sb_5. Above T_{CDW}, the field-dependent ρ_{xy} exhibits a linear behavior that can be well explained by a single-band model [14,15]. The extracted Hall coefficient (R_H) and carrier density (n_e) (Fig. S3 in the SM [44]) also prove it. Below T_{CDW}, an antisymmetric sideways S line shape gradually appears in the low-field region, indicating the emergence of the AHE [15]. Figures 1(e)–1(h) shows the field-dependent Hall resistivities at different temperatures in different $Cs(V_{1-x}Mo_x)_3Sb_5$ samples. With increasing Mo-doping level, the amplitude of the AHE in the low-field region, which is defined by the deviation from linear behavior, gradually decreases and finally vanishes above $x = 0.07$. By subtracting the linear background from the ordinary Hall term, an evident S shape due to the AHE can be seen [Fig. 1(i)]. This result indicates that, although T_{CDW} is increased by increasing Mo doping, the contribution of the AHE to the total Hall effect is significantly suppressed, like that in other doped cases [34,36,37]. Theoretically, the chiral flux phase has been proposed as a possible 2×2 charge-order-breaking time-reversal symmetry that explains the AHE in AV_3Sb_5 by involving intrinsic Berry curvature [22]. In previous studies on $Cs(V_{1-x}B_x)_3Sb_5$ (B = Ti, Cr, Nb) and pressurized CsV_3Sb_5 [15,34–40], the AHE emerges only below T_{CDW} and becomes weaker as the CDW is suppressed, which is consistent with the expectation of the chiral CDW picture. Within the same physical picture, the increase in T_{CDW} in Mo-doped CsV_3Sb_5 should enhance the AHE. However, this is inconsistent with the present observation, suggesting a possible change in the CDW state by introducing Mo doping. As reported in Sn-doped and pressurized CsV_3Sb_5, the CDW state can be changed by increasing the Sn-doping level or pressure [30,43]. Whether the CDW state is also changed should be key to understanding the disappearance of the AHE in $Cs(V_{1-x}Mo_x)_3Sb_5$.

The evolution of the CDW state in the Mo-doped cases were further studied using ^{51}V NMR measurements, a method proven to be sensitive to changes in CDW state [30,46]. These measurements were performed at 2 K, on the single-crystal samples at $x = 0.005$, 0.011, 0.02, and 0.05. As shown in Fig. 2(a), the spectral weight gradually shifts from the low-frequency peak to the high-frequency peak with increasing Mo doping, resulting in an asymmetric line shape of the full NMR spectra. To comprehend the change in the NMR spectra, we conducted a systematic temperature-dependent NMR measurement on $Cs(V_{0.95}Mo_{0.05})_3Sb_5$ in Fig. 2(b). The single NMR transition line above T_{CDW} is consistent with the perfect kagome network formed by the V sublattice [47–49].

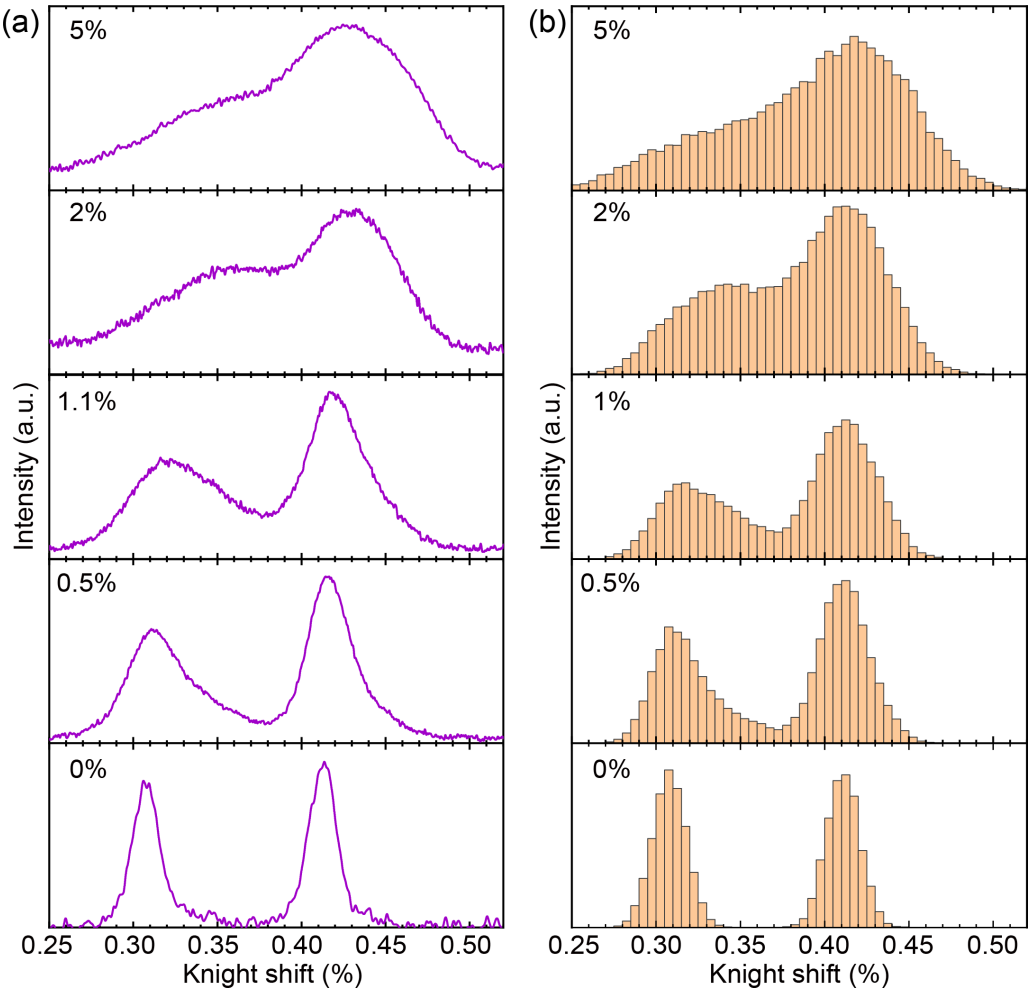

FIG. 3. (a) Mo-doping-dependent nuclear magnetic resonance (NMR) spectra at 2 K with an external magnetic field $\mu_0 H = 12$ T along the crystalline c axis. (b) The simulation of the NMR spectrum with different doping level.

Below T_{CDW}, the NMR transition line splits into two lines, indicating the appearance of the in-plane triple-Q CDW with a 2×2 superlattice. As shown in Fig. S4 in the SM [44], the sudden jump in the temperature-dependent splitting of the Knight shift indicates a first-order CDW transition, which is consistent with the pristine sample [48,49]. With further decreasing temperature [Fig. 2(b)], the spectral weight is gradually shifted from the low- to the high-frequency peak. On the other hand, Fig. 2(c) shows the Knight shift K of the $Cs(V_{0.95}Mo_{0.05})_3Sb_5$ is quantitatively identical to that of CsV_3Sb_5 above T_{CDW}. Here, $K = \frac{f-\gamma\hbar\mathbf{H}_0}{\gamma\hbar\mathbf{H}_0}$, where f is the resonance frequency obtained by NMR measurement, γ is the gyromagnetic ratio, $\hbar$ is the reduced Planck constant, and $\mathbf{H}_0$ is the external magnetic field. This suggests that K is insensitive to the impurity effect induced by doping, and the shift in spectral weight cannot be explained by the impurity effect. These results are unexpected for the original triple-Q CDW phase [47–49], indicating a significant change in the CDW modulation in $Cs(V_{0.95}Mo_{0.05})_3Sb_5$. Moreover, the measurements of magnetic susceptibility and specific heat coefficients (Fig. S2 in the SM [44]) do not show any evidence for another phase transition between different CDW phases below T_{CDW}, which rules out the long-range CDW order. Considering that NMR is a local probe, the asymmetric line shape of the NMR spectra in the Mo-doped sample should be ascribed to the development of a new kind of short-range CDW modulation.

Our previous work in pressurized CsV_3Sb_5 revealed that the formation of stripelike CDW leads to a characteristic shift of the NMR spectral weight to the high-frequency side [30], which is like the observed asymmetric spectra in $Cs(V_{0.95}Mo_{0.05})_3Sb_5$ (Fig. S5 in the SM [44]). Considering the larger size of the Mo atom than the V atom, Mo doping here would potentially introduce local lattice distortion that might be important for the formation of short-range stripelike CDW. As such, one candidate for such a short-range CDW modulation is stripelike CDW modulation like that in pressurized or Sn-doped CsV_3Sb_5 [30,43]. Consequently, we assume that the stripelike CDW is induced by the doped Mo atoms and simulate the doping-dependent NMR spectra (see Appendix). Comparing the experimental and simulated NMR spectra presented in Figs. 3(a) and 3(b), with the increasing of the Mo doping, the spectral weight shifts from the low- to the high-frequency peak, while the asymmetry line shape [Fig. 3(a)] is replicated in the simulation [Fig. 3(b)]. This implies that the doping effect is captured by the simulation, which can be explained by the continued enhancement of the local stripelike

TABLE I. The simulation parameters for different doping level. In our model, the emergence of stripelike CDW is locally triggered by Mo doping. For the CsV_3Sb_5 parent compound, due to the absence of the Mo impurity, cut1 and cut2 are meaningless.

Doping level (%)	0	0.5	1	2	5
cut1	1	0.4	0.4	0.6	0.7
cut2	1	0.1	0.1	0.2	0.6
Linewidth (kHz)	20	24	28	38	58

CDW. As shown in Table I, the simulation parameters cut1 and cut2 gradually increase with the increasing of the doping level. (Here, cut1 is anticorrelated with the correlation length of the stripelike CDW, and cut2 is related to the correlation length of the triple-Q CDW.) In our model, the emergence of the stripelike CDW is locally triggered by Mo doping. As the concentration of the Mo increases, the stripelike CDWs induced by different Mo atoms overlap. The inconsistent orientations of the stripes impede the formation of local stripelike CDW, causing the short-range CDW to become even shorter, which may raise cut1. Meanwhile, the increasing of cut2 may result from the enhancement of the CDW.

To visualize the evolution of the CDW states, the schematic plot of the simulated triple-Q CDW [Fig. 4(a)], stripelike CDW [Fig. 4(b)], and undistorted kagome states [Fig. 4(c)] is the same as the result in previous works [30] (for more detail about different CDW states, see Fig. S6 in the SM [44]), where the color represents the Knight shift of each sites. Meanwhile, the simulated topographies for different Mo-doping levels are shown in Figs. 4(d)–4(g). Upon further Mo doping, while the area of one short-range CDW patch around the Mo impurity becomes smaller, the total area of the CDW part of the sample increases because of a larger number of Mo sites. All these results indicate that the evolution of the NMR spectra in $Cs(V_{1-x}Mo_x)_3Sb_5$ can be attributed to the continuous augmentation of the short-range stripelike CDW.

Next, we also measured the temperature-dependent nuclear spin-lattice relaxation rate ($1/T_1$) for $Cs(V_{0.95}Mo_{0.05})_3Sb_5$. As shown in Fig. 5(a), below T_{CDW}, $1/T_1T$ for both NMR splitting lines decreases dramatically. The value of $1/T_1T$ for both V(I) and V(II) sites drops to half of that in pristine CsV_3Sb_5 at low temperatures. It should be noted that a similar suppression of $1/T_1T$ also occurs in pressurized CsV_3Sb_5 when the stripelike CDW emerges [30]. In addition, the absence of a clear transition between triple-Q CDW and stripelike CDW in the temperature-dependent $1/T_1T$ below T_{CDW} further supports a short-range stripelike CDW at low temperatures. Generally, for a Fermi liquid, the Knight shift K_{spin} and $1/T_1T$ should obey the so-called Korringa relation $K_{spin}^2 \propto \frac{1}{T_1T}$ (Fig. S7 in the SM [44]). As shown in Fig. 2(c), above T_{CDW}, although the temperature-dependent Knight shift is quantitatively the same as that in pristine CsV_3Sb_5 [48], the temperature-dependent $1/T_1T$ [Fig. 5(a)] is clearly suppressed compared with that in the pristine sample. Based on the discussion above, the origin of $1/T_1T$ above T_{CDW} is beyond a simple Fermi liquid, and additional contribution from magnetic fluctuations

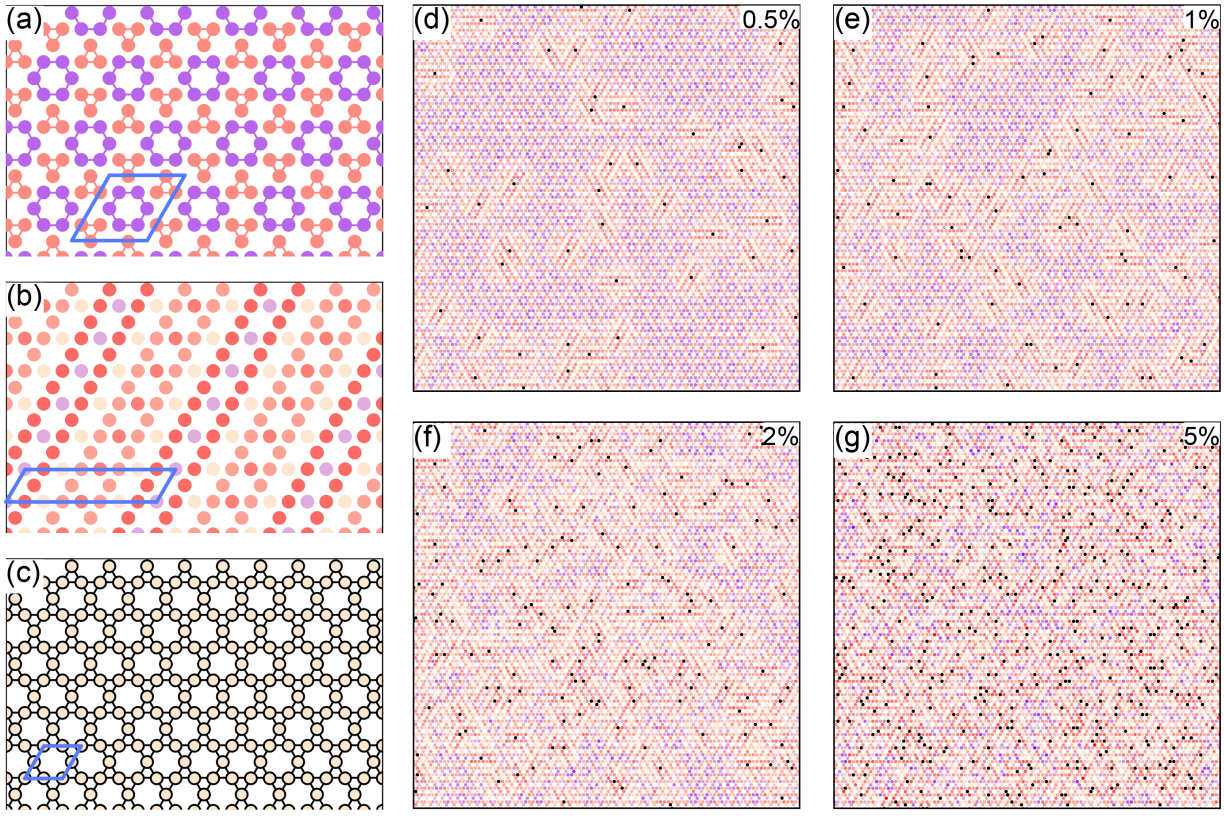

FIG. 4. Schematic plots of (a) triple-Q charge density wave (CDW), (b) stripelike CDW, and (c) undistorted kagome states in real space. The blue line indicates the unit cell of each state. (d)–(g) The simulated topography of V (colored) and Mo (black) atoms.

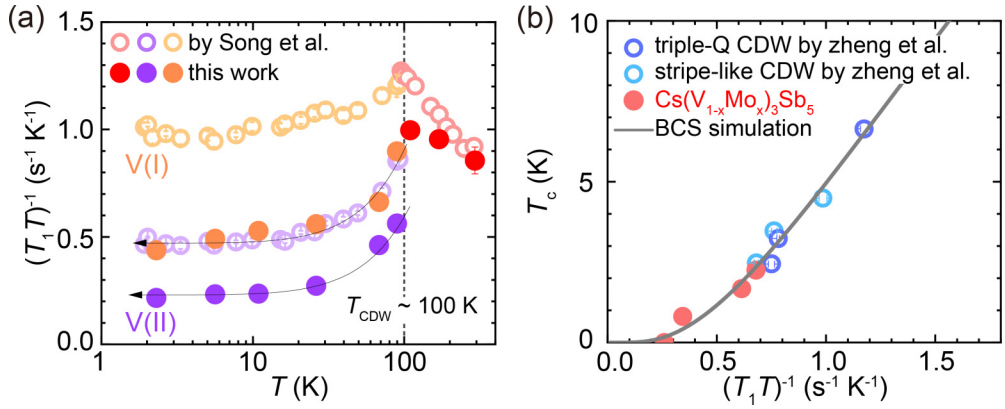

FIG. 5. (a) Temperature-dependent spin-lattice relaxation rate divided by T ($1/T_1T$) for $Cs(V_{0.95}Mo_{0.05})_3Sb_5$. The open dots are data for pristine CsV_3Sb_5 obtained in a previous study [48]. Below T_{CDW}, the definition of the V(I) (yellow) and V(II) (violet) sites is the same as in Fig. 2. (b) Correlation between T_c and $1/T_1T$. The blue and cyan dots were obtained in a previous study [30]. The red dot represents the $1/T_1T$ of Mo-doped CsV_3Sb_5 at 2 K, which is calculated by the average of $1/T_1T$ measured on each peak with its spectrum weight. The solid gray line is the BCS fitting in the weak-coupling region.

should be considered (Fig. S7 in the SM [44]). In fact, in pressurized CsV_3Sb_5, when the CDW transition is totally suppressed above $P_{c2} \sim 2.0$ GPa, the magnetic fluctuations lead to a persistent Curie-Weiss-like behavior in the temperature-dependent $1/T_1T$ [30]. Understanding the origin of emergent magnetic fluctuations in AV_3Sb_5 remains a challenging issue.

III. DISCUSSION

Thus far, our results demonstrate that Mo doping results in a change in the CDW from the original triple-Q CDW to a short-range stripelike CDW. This finding naturally explains the disappearance of the AHE in the original triple-Q CDW state. Moreover, the NMR results confirm that the absence of SC in Mo-doped CsV_3Sb_5 is tied to the emergence of the short-range stripelike CDW. Combined with previous work in $CsV_3Sb_{5-x}Sn_x$ and pressurized CsV_3Sb_5 [30,43], these results suggest that, regardless of whether the stripelike CDW order is long/short ranged or commensurate/incommensurate, it always exhibits a strong competition with SC in CsV_3Sb_5. In pressurized CsV_3Sb_5, our previous NMR measurements revealed a linear relationship between $1/T_1T$ and T_c in different CDW states [30]. Here, we try to use a weak-coupling BCS formula $T_c = 1.14\Theta_D \exp[-\frac{1}{N(0)V}]$ to explain such a linear behavior (for more details, see Sec. VIII in the SM [44]), in which $N(0)$ is assumed to be proportional to $(1/T_1T)^{1/2}$. As shown in Fig. 5(b), the weak-coupling BCS formula well explains the previous linear behavior. In the Mo-doped case, due to the emergence of the short-range stripelike CDW, the weighted average of $1/T_1T$ at 2 K in $Cs(V_{0.95}Mo_{0.05})_3Sb_5$ drops to half of that in pristine CsV_3Sb_5 [Fig. 5(a)]. Here, we measured the frequency-dependent $1/T_1T$ at 2 K, and the intensity of each frequency was employed as the weighting factor to calculate the weighted average of $1/T_1T$. Following the weak-coupling BCS formula [Fig. 5(b)], it can naturally explain the vanished SC. Additionally, the $1/T_1T$ value across multiple Mo-doped CsV_3Sb_5 samples can be accurately predicted using the same weak-coupling BCS formula. These results suggest that the density of states at the Fermi level plays a key role in the competition between the stripelike CDW and SC. Notably, as suggested by the Cr-doping case, the magnetic impurities introduced by Cr substitution may break the Cooper pair [36]. Similarly, Mo ions with $4d^3$ electron configuration could also introduce magnetic impurities that break the Cooper pair. Generally, NMR measurement is sensitive to the magnetic impurity. As extensively presented in cases of dilute alloy [50–52], the impurity relaxation ought to generate a Curie tail in $1/T_1T$. In contrast, the observation of flattened $1/T_1T$ in $Cs(V_{0.95}Mo_{0.05})_3Sb_5$ [Fig. 5(a)] indicates a reduced role of magnetic impurity in SC attenuation. This is also supported by the linewidth results (Fig. S8(a) in the SM [44]). Moreover, the magnetic susceptibility also shows a doping-independent magnetic impurity concentration (Figs. S8(b) and S8(c) in the SM [44]). In this sense, the suppression of SC in the stripelike CDW mainly results from the dramatic change in the density of states at the Fermi level. Finally, a similar physical picture could also be used to reconcile various superconducting behaviors for different doping cases [30–41], which calls for further investigation in different doping systems.

IV. CONCLUSIONS

In conclusion, we successfully synthesized high-quality $Cs(V_{1-x}Mo_x)_3Sb_5$ single crystals with a maximum doping level of $x = 0.083$ and revealed the competitive behavior between the CDW and SC. By a comprehensive study with resistivity, Hall effect, and ^{51}V NMR measurements, we illuminated that the competition between the CDW and SC results from the emergence of the short-ranged stripelike CDW, which also explains the disappearance of the AHE. Moreover, further investigation of the nuclear spin-lattice relaxation rate on the CDW state in Mo-doped CsV_3Sb_5 indicates that the short-range stripelike CDW state strongly suppresses the density of states at the Fermi level, which provides a self-consistent explanation for the competitive behavior between the CDW and SC. Our present results are helpful for clarifying the exotic nature of the CDW in kagome superconductors AV_3Sb_5.

ACKNOWLEDGMENTS

This paper is supported by the National Key R&D Program of China (Grant No. 2022YFA1602601), the National Natural Science Foundation of China (Grants No. 11888101, No. 12034004, No. 12004365, No. 12074364, and No. 12161160316), the Strategic Priority Research Program of Chinese Academy of Sciences (Grant No. XDB25000000), the Basic Research Program of the Chinese Academy of Sciences Based on Major Scientific Infrastructures (Grant No. JZHKYPT-2021–08), the CAS Project for Young Scientists in Basic Research (Grant No. 2022YSBR-048), the Anhui Initiative in Quantum Information Technologies (Grant No. AHY160000), and the Innovation Program for Quantum Science and Technology (Grant No. 2021ZD0302800).

APPENDIX: MATERIALS AND METHODS

1. Crystal growth and characterization

Crystal growth of $Cs(V_{1-x}Mo_x)_3Sb_5$ was achieved with an excess of CsSb which acts as a self-flux in this case. High-purity elements of Cs, V, Mo, and Sb were mixed in a molar ratio of $2:1-x:x:6$ in an alumina crucible and placed into a tantalum container. Then the tantalum container was sealed inside an evacuated quartz tube. The tubes were heated to 1000 °C at a rate of 100 °C/h, held there for 20 h, and then cooled to 650 °C at a rate of 2 °C/h. The flux is removed by centrifugation, and shiny crystals are obtained.

The crystal structure was characterized by a powder x-ray diffractometer (SmartLab-9, Rigaku Corp.) with Cu $K\alpha$ radiation (Fig. S9 in the SM [44]). The chemical composition was identified on a Carl Zeiss Microscopy Ltd. scanning electron microscope (Sigma 500) equipped with energy-dispersive x-ray spectroscopy (Fig. S10 in the SM [44]). The resistivity measurement is carried out by a Physical Properties Measurement System (Quantum Design PPMS). The Hall resistivity was measured using the five-probe method with the current flowing in the ab plane and a magnetic field applied along the c axis. The magnetic susceptibility is measured by a superconducting quantum interference device magnetometer (Quantum Design MPMS3).

2. NMR measurements

A commercial NMR spectrometer from Thamway Co. Ltd. was used for NMR measurements. Here, ^{51}V NMR experiments were performed on a single-crystal sample at a fixed 12 Tesla magnetic field along the c axis. The external magnetic field is calibrated by ^{63}Cu NMR with the sample coil. Here, ^{121}Sb nuclear quadrupole resonance (NQR) spectra were measured on the same coil and sample. All NMR and NQR spectra are acquired by the standard spin-echo method with a fast Fourier transform sum.

For ^{51}V, the nuclear spin number is $I=\frac{7}{2}$, and the gyromagnetic ratio γ_N is 11.193 MHz/T. The NMR spectra split into $2I$ transition lines separated by a so-called quadrupole frequency ($\upsilon_{\alpha\alpha}$). Considering only the first-order perturbation of the quadrupole interaction, the resonance frequency for different transition lines follows:

$$\begin{aligned}\nu &= \nu_0 + \nu^{(1)}_{m,\,m-1}\\ &= \nu_0 + \tfrac{1}{2}\nu_Q\big(m-\tfrac{1}{2}\big)(3\cos^2\theta - 1 - \eta\sin^2\theta\cos 2\phi) \quad \text{(A1)}\end{aligned}$$

Here, ν_0 is the Larmor frequency of the central peak, $\nu_Q = \frac{3eQV_{zz}}{2I(2I-1)\hbar}$ is the quadrupole frequency in the z principal axis of the EFG tensor, m is the z-axis spin number, $\theta(\phi)$ is the polar (azimuthal) angle between the external field $\mathbf{H}_0$ and the principal axis of the EFG tensor, and η is the asymmetry parameter, defined as $\eta = |\frac{V_{xx}-V_{yy}}{V_{zz}}|$, where $|V_{xx}| \leqslant |V_{yy}| \leqslant |V_{zz}|$ are the three principal components of the EFG tensor. The equation gives the frequency interval between adjacent m equal to $|\frac{1}{2}\nu_Q(3\cos^2\theta - 1 - \eta\sin^2\theta\cos 2\phi)|$, which corresponds to the frequency interval of adjacent peaks in the NMR spectrum.

The nuclear spin-lattice relaxation time (T_1) is fitted by the inverse recovery method and fitting the recovery of the nuclear magnetization $M(t)$ to a function with $1-\frac{M(t)}{M(\infty)} = I_0\{\frac{1}{84}\times\exp[-(\frac{t}{T_1})^\beta] + \frac{3}{44}\times\exp[-(\frac{6t}{T_1})^\beta] + \frac{75}{364}\times\exp[-(\frac{15t}{T_1})^\beta] + \frac{1225}{1716}\times\exp[-(\frac{28t}{T_1})^\beta]\}$, in which error bars are determined by the least-square method.

3. Spectra simulation

The simulation of the doping-dependent NMR spectra based on three assumptions:

(a) First, the stripelike CDW competes with the triple-Q CDW, and the Knight shift in Mo-doped CsV_3Sb_5 can be expressed as $K(\vec{r}) = dK_{3Q}(1-\lambda) + dK_{4a}\lambda + K_0$, where dK_{3Q} is the relative Knight shift of the triple-Q CDW in CsV_3Sb_5, and dK_{4a} is that for the stripelike CDW in CsV_3Sb_5 at 1.05 GPa. Both Knight shifts are related to the central Knight shift K_0, which is the average of the two NMR peaks in CsV_3Sb_5 at 2 K. Here, λ denotes the strength of the stripelike CDW.

(b) Secondly, the Mo atoms induce the stripelike CDW, the strength of which decays exponentially as the distance from the impurity increases. Accordingly, λ should depend on the ion coordinates $\vec{r}$, as represented by $\lambda(\vec{r}, \overrightarrow{r_{im}}) = \exp[-\frac{(\vec{r}-\overrightarrow{r_{im}})^2}{5a_0^2}]$, where $\overrightarrow{r_{im}}$ is the coordinate of the V atoms with respect to the nearest-neighbor Mo impurity, and a_0 is the lattice constant. We have also defined two kinds of cutoff points (noted as cut1 and cut2). When $\lambda(\vec{r}, \overrightarrow{r_{im}}) >$ cut1, we presume the CDW is dominated by the stripe and $\lambda(\vec{r}, \overrightarrow{r_{im}}) = 1$. When $\lambda(\vec{r}, \overrightarrow{r_{im}}) <$ cut2, we presume the CDW is dominated by the triple-Q and $\lambda(\vec{r}, \overrightarrow{r_{im}}) = 0$.

(c) Thirdly, the linewidth broadening is proportional to the Mo doping, and the linewidth is broadened with the Gauss function.

The simulation parameters are shown in Table I.

[1] F. Pollmann, P. Fulde, and K. Shtengel, Kinetic ferromagnetism on a kagome lattice, Phys. Rev. Lett. **100**, 136404 (2008).

[2] W. H. Ko, P. A. Lee, and X. G. Wen, Doped kagome system as exotic superconductor, Phys. Rev. B **79**, 214502 (2009).

[3] A. O'Brien, F. Pollmann, and P. Fulde, Strongly correlated fermions on a kagome lattice, Phys. Rev. B **81**, 235115 (2010).

[4] M. L. Kiesel and R. Thomale, Sublattice interference in the kagome Hubbard model, Phys. Rev. B **86**, 121105(R) (2012).

[5] S. L. Yu and J. X. Li, Chiral superconducting phase and chiral spin-density-wave phase in a Hubbard model on the kagome lattice, Phys. Rev. B **85**, 144402 (2012).

[6] W.-S. Wang, Z.-Z. Li, Y.-Y. Xiang, and Q.-H. Wang, Competing electronic orders on kagome lattices at van Hove filling, Phys. Rev. B **87**, 115135 (2013).

[7] M. L. Kiesel, C. Platt, and R. Thomale, Unconventional Fermi surface instabilities in the kagome Hubbard model, Phys. Rev. Lett. **110**, 126405 (2013).

[8] B. R. Ortiz, L. C. Gomes, J. R. Morey, M. Winiarski, M. Bordelon, J. S. Mangum, I. W. H. Oswald, J. A. Rodriguez-Rivera, J. R. Neilson, S. D. Wilson *et al.*, New kagome prototype materials: Discovery of KV_3Sb_5, RbV_3Sb_5, and CsV_3Sb_5, Phys. Rev. Mater. **3**, 094407 (2019).

[9] B. R. Ortiz, S. M. L. Teicher, Y. Hu, J. L. Zuo, P. M. Sarte, E. C. Schueller, A. M. M. Abeykoon, M. J. Krogstad, S. Rosenkranz, R. Osborn *et al.*, CsV_3Sb_5: A $\mathbb{Z}_2$ topological kagome metal with a superconducting ground state, Phys. Rev. Lett. **125**, 247002 (2020).

[10] Q. W. Yin, Z. J. Tu, C. S. Gong, Y. Fu, S. H. Yan, and H. C. Lei, Superconductivity and normal-state properties of kagome metal RbV_3Sb_5 single crystals, Chin. Phys. Lett. **38**, 037403 (2021).

[11] T. Neupert, M. M. Denner, J.-X. Yin, R. Thomale, and M. Z. Hasan, Charge order and superconductivity in kagome materials, Nat. Phys. **18**, 137 (2022).

[12] T. Nguyen and M. Li, Electronic properties of correlated kagomé metals AV_3Sb_5 (A = K, Rb, and Cs): A perspective, J. Appl. Phys. **131**, 060901 (2022).

[13] K. Jiang, T. Wu, J.-X. Yin, Z. Wang, M. Z. Hasan, S. D. Wilson, X. Chen, and J. Hu, Kagome superconductors AV_3Sb_5 (A = K, Rb, Cs), Natl. Sci. Rev. **10**, nwac199 (2023).

[14] S. Y. Yang, Y. Wang, B. R. Ortiz, D. Liu, J. Gayles, E. Derunova, R. Gonzalez-Hernandez, L. Šmejkal, Y. Chen, S. S. P. Parkin *et al.*, Giant, unconventional anomalous Hall effect in the metallic frustrated magnet candidate, KV_3Sb_5, Sci. Adv. **6**, eabb6003 (2020).

[15] F. H. Yu, T. Wu, Z. Y. Wang, B. Lei, W. Z. Zhuo, J. J. Ying, and X. H. Chen, Concurrence of anomalous Hall effect and charge density wave in a superconducting topological kagome metal, Phys. Rev. B **104**, L041103 (2021).

[16] L. Yu, C. Wang, Y. Zhang, M. Sander, S. Ni, Z. Lu, S. Ma, Z. Wang, Z. Zhao, H. Chen *et al.*, Evidence of a hidden flux phase in the topological kagome metal CsV_3Sb_5, arXiv:2107.10714.

[17] C. Mielke, D. Das, J.-X. Yin, H. Liu, R. Gupta, Y.-X. Jiang, M. Medarde, X. Wu, H. C. Lei, J. Chang *et al.*, Time-reversal symmetry-breaking charge order in a kagome superconductor, Nature (London) **602**, 245 (2022).

[18] Z. Guguchia, C. Mielke, D. Das, R. Gupta, J.-X. Yin, H. Liu, Q. Yin, M. H. Christensen, Z. Tu, C. Gong *et al.*, Tunable unconventional kagome superconductivity in charge ordered RbV_3Sb_5 and KV_3Sb_5, Nat Commun. **14**, 153 (2023).

[19] Y.-X. Jiang, J.-X. Yin, M. M. Denner, N. Shumiya, B. R. Ortiz, G. Xu, Z. Guguchia, J. He, M. S. Hossain, X. Liu *et al.*, Unconventional chiral charge order in kagome superconductor KV_3Sb_5, Nat. Mater. **20**, 1353 (2021).

[20] Z. Wang, Y.-X. Jiang, J.-X. Yin, Y. Li, G.-Y. Wang, H.-L. Huang, S. Shao, J. Liu, P. Zhu, N. Shumiya *et al.*, Electronic nature of chiral charge order in the kagome superconductor CsV_3Sb_5, Phys. Rev. B **104**, 075148 (2021).

[21] N. Shumiya, M. S. Hossain, J.-X. Yin, Y.-X. Jiang, B. R. Ortiz, H. Liu, Y. Shi, Q. Yin, H. Lei, S. S. Zhang *et al.*, Intrinsic nature of chiral charge order in the kagome superconductor RbV_3Sb_5, Phys. Rev. B **104**, 035131 (2021).

[22] X. Feng, K. Jiang, Z. Wang, and J. Hu, Chiral flux phase in the Kagome superconductor AV_3Sb_5, Sci. Bull. **66**, 1384 (2021).

[23] C. M. Varma, Pseudogap in cuprates in the loop-current ordered state, J. Phys. Condens. Matter **26**, 505701 (2014).

[24] Q. Wu, Z. X. Wang, Q. M. Liu, R. S. Li, S. X. Xu, Q. W. Yin, C. S. Gong, Z. J. Tu, H. C. Lei, T. Dong *et al.*, Simultaneous formation of two-fold rotation symmetry with charge order in the kagome superconductor CsV_3Sb_5 by optical polarization rotation measurement, Phys. Rev. B **106**, 205109 (2022).

[25] Y. Xu, Z. Ni, Y. Liu, B. R. Ortiz, Q. Deng, S. D. Wilson, B. Yan, L. Balents, and L. Wu, Three-state nematicity and magneto-optical Kerr effect in the charge density waves in kagome superconductors, Nat. Phys. **18**, 1470 (2022).

[26] Y. Hu, S. Yamane, G. Mattoni, K. Yada, K. Obata, Y. Li, Y. Yao, Z. Wang, J. Wang, C. Farhang *et al.*, Time-reversal symmetry breaking in charge density wave of CsV_3Sb_5 detected by polar Kerr effect, arXiv:2208.08036.

[27] D. R. Saykin, C. Farhang, E. D. Kountz, D. Chen, B. R. Ortiz, C. Shekhar, C. Felser, S. D. Wilson, R. Thomale, J. Xia *et al.*, High resolution polar Kerr effect studies of CsV_3Sb_5: Tests for time-reversal symmetry breaking below the charge-order transition, Phys. Rev. Lett. **131**, 016901 (2023).

[28] Y. Xiang, Q. Li, Y. Li, W. Xie, H. Yang, Z. Wang, Y. Yao, and H.-H. Wen, Twofold symmetry of c-axis resistivity in topological kagome superconductor CsV_3Sb_5 with in-plane rotating magnetic field, Nat. Commun. **12**, 6727 (2021).

[29] L. Nie, K. Sun, W. Ma, D. Song, L. Zheng, Z. Liang, P. Wu, F. Yu, J. Li, M. Shan *et al.*, Charge-density-wave-driven electronic nematicity in a kagome superconductor, Nature (London) **604**, 59 (2022).

[30] L. X. Zheng, Z. M. Wu, Y. Yang, L. P. Nie, M. Shan, K. L. Sun, D. W. Song, F. H. Yu, J. Li, D. Zhao *et al.*, Emergent charge order in pressurized kagome superconductor CsV_3Sb_5, Nature (London) **611**, 682 (2022).

[31] K. Y. Chen, N. N. Wang, Q. W. Yin, Y. H. Gu, K. Jiang, Z. J. Tu, C. S. Gong, Y. Uwatoko, J. P. Sun, H. C. Lei *et al.*, Double superconducting dome and triple enhancement of T_c in the Kagome superconductor CsV_3Sb_5 under high pressure, Phys. Rev. Lett. **126**, 247001 (2021).

[32] F. H. Yu, D. H. Ma, W. Z. Zhuo, S. Q. Liu, X. K. Wen, B. Lei, J. J. Ying, and X. H. Chen, Unusual competition of superconductivity and charge-density-wave state in a compressed topological kagome metal, Nat. Commun. **12**, 3645 (2021).

[33] Y. M. Oey, B. R. Ortiz, F. Kaboudvand, J. Frassineti, E. Garcia, R. Cong, S. Sanna, V. F. Mitrović, R. Seshadri, and S. D. Wilson, Fermi level tuning and double-dome superconductivity in the kagome metal $CsV_3Sb_{5-x}Sn_x$, Phys. Rev. Mater **6**, L041801 (2022).

[34] H. Yang, Z. Huang, Y. Zhang, Z. Zhao, J. Shi, H. Luo, L. Zhao, G. Qian, H. Tan, B. Hu *et al.*, Titanium doped kagome superconductor $CsV_{3-x}Ti_xSb_5$ and two distinct phases, Sci. Bull. **67**, 2176 (2022).

[35] Y. Liu, Y. Wang, Y. Cai, Z. Hao, X.-M. Ma, L. Wang, C. Liu, J. Chen, L. Zhou, J. Wang *et al.*, Doping evolution of superconductivity, charge order and band topology in holedoped topological kagome superconductors $Cs(V_{1-x}Ti_x)_3Sb_5$, Phys. Rev. Mater. **7**, 064801 (2023).

[36] G. F. Ding, H. L. Wo, Y. Q. Gu, Y. M. Gu, and J. Zhao, Effect of chromium doping on superconductivity and charge density wave order in the kagome metal $Cs(V_{1-x}Cr_x)_3Sb_5$, Phys. Rev. B **106**, 235151 (2022).

[37] Y. Li, Q. Li, X. Fan, J. Liu, Q. Feng, M. Liu, C. Wang, J.-X. Yin, J. Duan, X. Li *et al.*, Tuning the competition between superconductivity and charge order in the kagome superconductor $Cs(V_{1-x}Nb_x)_3Sb_5$, Phys. Rev. B **105**, L180507 (2022).

[38] T. Kato, Y. Li, K. Nakayama, Z. Wang, S. Souma, F. Matsui, M. Kitamura, K. Horiba, H. Kumigashira, T. Takahashi *et al.*, Fermiology and origin of T_c enhancement in a Kagome superconductor $Cs(V_{1-x}Nb_x)_3Sb_5$, Phys. Rev. Lett. **129**, 206402 (2022).

[39] J. Li, W. Xie, J. J. Liu, Q. Li, X. Li, H. Yang, Z. W. Wang, Y. G. Yao, and H.-H. Wen, Strong-coupling superconductivity and weak vortex pinning in Ta-doped CsV_3Sb_5 single crystals, Phys. Rev. B **106**, 214529 (2022).

[40] Y. Zhong, J. Liu, X. Wu, Z. Guguchia, J.-X. Yin, A. Mine, Y. Li, S. Najafzadeh, D. Das, C. Mielke *et al.*, Nodeless electron pairing in CsV_3Sb_5-derived kagome superconductors, Nature (London) **617**, 488 (2023).

[41] M. Liu, T. Han, X. Hu, Y. Tu, Z. Zhang, M. Long, X. Hou, Q. Mu, and L. Shan, Evolution of superconductivity and charge density wave through Ta and Mo doping in CsV_3Sb_5, Phys. Rev. B **106**, L140501 (2022).

[42] P. Wu, Y. Tu, Z. Wang, S. Yu, H. Li, W. Ma, Z. Liang, Y. Zhang, X. Zhang, Z. Li *et al.*, Unidirectional electron-phonon coupling in the nematic state of a kagome superconductor, Nat. Phys. **19**, 1143 (2023).

[43] L. Kautzsch, Y. M. Oey, H. Li, Z. Ren, B. R. Ortiz, G. Pokharel, R. Seshadri, J. Ruff, T. Kongruengkit, J. W. Harter *et al.*, Incommensurate charge-stripe correlations in the kagome superconductor $CsV_3Sb_{5-x}Sn_x$, npj Quantum Mater. **8**, 37 (2023).

[44] See Supplemental Material at http://link.aps.org/supplemental/10.1103/PhysRevResearch.6.023295 for Figs. S1–S8 and which includes Refs. [30,45,48,53].

[45] F. H. Yu, X. K. Wen, Z. G. Gui, T. Wu, Z. Wang, Z. J. Xiang, J. J. Ying, and X. H. Chen, Pressure tuning of the anomalous Hall effect in the kagome superconductor CsV_3Sb_5, Chin. Phys. B **31**, 017405 (2022).

[46] T. Wu, H. Mayaffre, S. Kramer, M. Horvatić, C. Berthier, W. N. Hardy, R. Liang, D. A. Bonn, and M.-H. Julien, Magnetic-field-induced charge-stripe order in the high-temperature superconductor $YBa_2Cu_3O_y$, Nature (London) **477**, 191 (2011).

[47] C. Mu, Q. Yin, Z. Tu, C. Gong, H. Lei, Z. Li, and J. Luo, S-wave superconductivity in kagome metal CsV_3Sb_5 revealed by $^{121/123}$Sb NQR and ^{51}V NMR measurements, Chin. Phys. Lett. **38**, 077402 (2021).

[48] D. W. Song, L. X. Zheng, F. H. Yu, J. Li, L. P. Nie, M. Shan, D. Zhao, S. J. Li, B. L. Kang, Z. M. Wu *et al.*, Orbital ordering and fluctuations in a kagome superconductor CsV_3Sb_5, Sci. China Phys. Mech. Astron. **65**, 247462 (2022).

[49] J. Luo, Z. Zhao, Y. Z. Zhou, J. Yang, A. F. Fang, H. T. Yang, H. J. Gao, R. Zhou, and G.-Q. Zheng, Possible star-of-David pattern charge density wave with additional modulation in the kagome superconductor CsV_3Sb_5, npj Quantum Mater. **7**, 30 (2022).

[50] B. Giovannini, P. Pincus, G. Gladstone, and A. J. Heeger, Nuclear relaxation in dilute magnetic alloys, J. Phys. Colloques **32**, C1 (1971).

[51] M. R. McHenry, B. G. Silbernagel, and J. H. Wernick, Nuclear spin-lattice relaxation in the $La_{1-c}Gd_cAl_2$ intermetallic compounds, Phys. Rev. B **5**, 2958 (1972).

[52] D. E. MacLaughlin, M. Daugherty, and K. Parvin, Nuclear spin-lattice relaxation and pair breaking in superconducting $(LaGd)Al_2$, Solid State Commun. **12**, 5 (1973).

[53] H. Tan, Y. Liu, Z. Wang, and B. Yan, Charge density waves and electronic properties of superconducting Kagome metals, Phys. Rev. Lett. **127**, 046401 (2021).